New Journal of Physics
The open access journal at the forefront of physics

Deutsche Physikalische Gesellschaft DPG IOP Institute of Physics

Sensitivity of the superconducting state and magnetic susceptibility to key aspects of electronic structure in ferropnictides

To cite this article: A F Kemper *et al* 2010 *New J. Phys.* **12** 073030

New Journal of Physics
The open-access journal for physics

Sensitivity of the superconducting state and magnetic susceptibility to key aspects of electronic structure in ferropnictides

A F Kemper[1,2,5,7], T A Maier[3], S Graser[4], H-P Cheng[5], P J Hirschfeld[5] and D J Scalapino[6]

[1] Stanford Institute for Materials and Energy Science, SLAC National Accelerator Laboratory, Menlo Park, CA 64025, USA
[2] Geballe Laboratory for Advanced Materials, Stanford University, Stanford, CA 94305, USA
[3] Center for Nanophase Materials Sciences and Computer Science and Mathematics Division, Oak Ridge National Laboratory, Oak Ridge, TN 37831-6494, USA
[4] Center for Electronic Correlations and Magnetism, Institute of Physics, University of Augsburg, D-86135 Augsburg, Germany
[5] Department of Physics, University of Florida, Gainesville, FL 32611, USA
[6] Department of Physics, University of California, Santa Barbara, CA 93106-9530, USA
E-mail: kemper@stanford.edu

New Journal of Physics **12** (2010) 073030 (23pp)
Received 21 March 2010
Published 23 July 2010
Online at http://www.njp.org/
doi:10.1088/1367-2630/12/7/073030

Abstract. Experiments on the iron–pnictide superconductors appear to show some materials where the ground state is fully gapped, and others where low-energy excitations dominate, possibly indicative of gap nodes. Within the framework of a five-orbital spin fluctuation theory for these systems, we discuss how changes in the doping, the electronic structure or interaction parameters can tune the system from a fully gapped to a nodal sign-changing gap with s-wave (A_{1g}) symmetry ($s^{\pm}$). In particular, we focus on the role of the hole pocket at the (π, π) point of the unfolded Brillouin zone, identified as crucial to the pairing by Kuroki *et al* (2009 *Phys. Rev.* B **79** 224511), and show that its presence leads to additional nesting of hole and electron pockets, which stabilizes the isotropic $s^{\pm}$ state. The pocket's contribution to the pairing can be tuned

[7] Author to whom any correspondence should be addressed.

by doping, surface effects and by changes in interaction parameters, which we examine. Analytic expressions for orbital pairing vertices calculated within the random phase approximation (RPA) fluctuation exchange approximation allow us to draw connections between aspects of the electronic structure, interaction parameters and the form of the superconducting gap.

Contents

1. Introduction

In any new class of superconductors, the structure of the order parameter is an important clue to the nature of the pairing mechanism, but the determination of this structure is seldom immediate. In cuprates, for example, many different types of experiments on a variety of samples had to be analyzed and compared before a consensus was achieved, and the experimental picture was not clarified until the effects of disorder were understood and clean samples were prepared. It is therefore not unexpected that the symmetry and momentum structure of the gap in Fe-based superconductors are still controversial nearly two years after their discovery [1]. Nevertheless, the range of behavior seen in different materials is striking [2]. Here we pose, from the point of view of a weak coupling fluctuation exchange theory [3, 4], the following questions. Is it possible that the superconducting state of the ferropnictides is intrinsically sensitive to aspects of the electronic structure that 'tune' the pairing interaction? If so, which degrees of freedom are most important?

Based on density functional theory (DFT) [5]–[7], quantum oscillations and angle-resolved photoemission experiments (ARPES) [8]–[13], the Fermi surface of the Fe-pnictides is believed to consist of a few small hole and electron pockets, as shown in figure 1, where we have also indicated the predominant Fe-orbital character of the various parts of the Fermi surface taken from the DFT calculations of Cao *et al* [7] for the LaFeAsO material. We will follow the convention in [4] and elsewhere and refer to the hole pockets around the $(0, 0)$ point as the α sheets and the electron pockets around the $(\pi, 0)$ and $(0, \pi)$ points of the unfolded (1-Fe) Brillouin zone as the β sheets. Early on, it was proposed by Mazin *et al* [14] and Dong *et al* [15] that the nested structure of this Fermi surface would lead to a peak in the magnetic susceptibility near $(\pi, 0)$ and that this might drive a sign change in the superconducting order parameter between the α and β sheets [14]. Several experiments on the Fe-based superconductors are

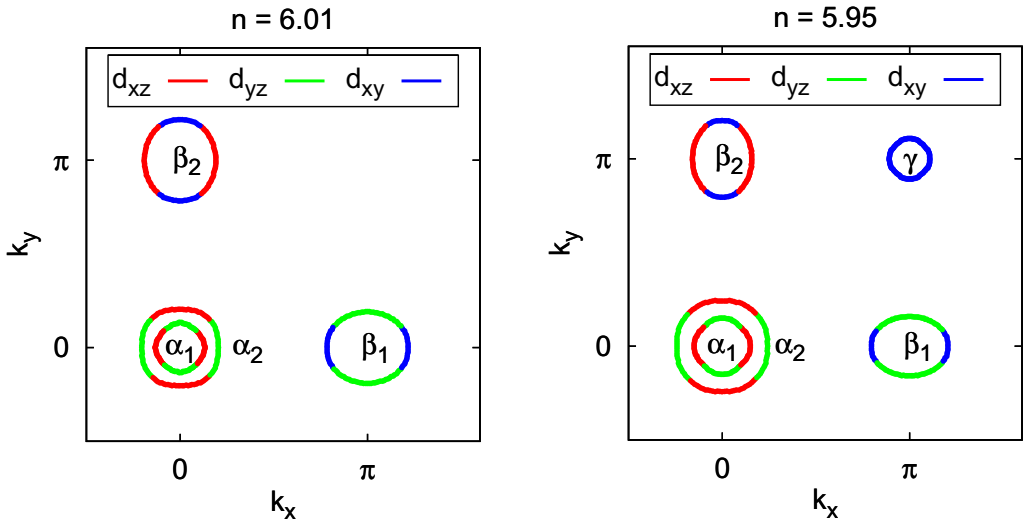

Figure 1. Fermi sheets of the five-band model for $n = 6.01$ (left) and $n = 5.95$ (right) with colors indicating majority orbital character (red $= d_{xz}$, green $= d_{yz}$, blue $= d_{xy}$). The γ Fermi surface sheet is a hole pocket that appears for $\sim$1% hole doping.

indeed consistent with a gap that is isotropic (independent of momentum on a given pocket), but possibly with overall sign change of this type. ARPES experiments, while not sensitive to the sign of the gap, are the most direct measure of its magnitude and have consistently provided evidence taken to support an isotropic gap structure in momentum space [8, 12]. The observation of a resonance in inelastic neutron scattering is strong evidence for a sign change of the superconducting gap [16]–[21].

However, many other experiments appear to support the existence of low-lying excitations below the apparent gap energy. For example, in both the LaFePO system [22, 23] and in $BaFe_2As_{1-x}P_x$ [24], a linear-T dependence of the low-T penetration depth $\Delta\lambda(T)$ has been reported, and in $Ba(Fe_{1-x}Co_x)_2As_2$, $\Delta\lambda$ varies close to T^2 over most of the phase diagram [25]; these power laws are in contrast to the activated temperature dependences expected for an isotropic gap. Similar power laws have been observed in NMR [26]–[31], thermal conductivity [24], [32]–[37] and Raman scattering [38]. One obvious way of interpreting these observations is to suppose that the superconducting gap has nodes on parts of the Fermi surface, allowing for the excitation of quasi-particles at arbitrarily low energies. However, one may also show that in an isotropic 'sign-changing s-wave' ($s^{\pm}$) superconductor, disorder can create subgap states [39] under certain conditions, depending on the ratio of inter- to intra-band impurity scattering. An impurity band at the Fermi level in an $s^{\pm}$ state will also lead to $\Delta\lambda \sim T^2$. There is no known scenario for producing $\Delta\lambda \sim T$ with impurity scattering in a gapped state, however. It is extremely important to establish whether low-energy excitations are intrinsic (nodal) or extrinsic (disorder-induced), and under what circumstances fully developed gaps, as opposed to highly anisotropic gaps, possibly with nodes, should be expected.

From the standpoint of fluctuation exchange theories of pairing based on realistic Fermi surfaces in these materials, the most likely states indeed appear to be preferentially of 's-wave' symmetry, with quasi-isotropic gaps on the hole pockets but highly anisotropic states

on the electron pockets [3, 4, 40]. All of these calculations indicate the proximity of other pairing channels, particularly the one with $d_{x^2-y^2}$ symmetry, but transitions between an s-wave state and a d-wave state would give rise to thermodynamic anomalies that have not yet been convincingly observed. Attention has therefore focused primarily on the possibility of s-wave (A_{1g} symmetry) states with 'accidental' nodes, i.e. nodes whose existence is due to details of the pairing interaction rather than symmetry. When the leading instability was of s-wave (A_{1g}) type, five-orbital calculations found highly anisotropic states for all values of the parameter space explored [4], in apparent contradiction to the existence of nearly isotropic states experimentally observed in some materials.

What aspects of the physics of these materials are responsible for the nodes or near-nodes seen in these theories? Some observations on this question have already been made. Maier *et al* [41] pointed out that, within a model with intra- and inter-orbital interactions, nodes were driven by the intra-orbital Coulomb repulsion, the scattering between the two β sheets neglected in simpler two-band approaches, and a tendency (observed for the parameters considered in that work which were consistent with local spin-rotational invariance (SRI)) of electrons in like orbitals to pair. Kuroki *et al* [42] made an important connection between the lattice structure, electronic structure and pairing state of the Fe-based superconductors, observing that in DFT calculations the pnictide atom height above the Fe plane appeared to control the appearance of a third γ Fermi surface sheet centered on the Γ point in the folded zone corresponding to a (π, π) pocket in the unfolded zone. This new hole-type pocket, not considered in [4], stabilizes a more isotropic $s^{\pm}$ state. When the γ pocket is present, intra-orbital $q \sim (\pi, 0)$ and $(0, \pi)$ scatterings of d_{xy} pairs between the γ and β pockets favor a nodeless $s^{\pm}$ state.

Within a model with band interactions, Vildosola *et al* [43] and Calderon *et al* [44] have also discussed the change in the electronic structure caused by the shift of the pnictogen. In particular, the latter authors have noted that a change in the angle α formed by the Fe–As bonds and the Fe-plane can modify the orbital content as well as the shape of the Fermi surface sheets. In a similar model, Chubukov *et al* [45] deduced a phase diagram manifesting a transition between a nodal and fully gapped state with s-symmetry as a function of a parameter controlling the relative importance of intraband repulsion, and Thomale *et al* [46] reached similar conclusions within a four-band model, exploring the stability of the nodeless state with respect to doping and other changes in electronic structure. Ikeda *et al* [47] considered the doping dependence of spin fluctuations and electron correlations within the renormalized fluctuation exchange (FLEX) approximation using LDA dispersions; they also observe anisotropic behavior of the gap function around the M point for the electron-doped material, and fully-gapped behavior in the hole-doped material. In a subsequent work, they explored the doping dependence of the pairing state within FLEX [48]. Wang *et al* [49] have also discussed the important role played by the γ Fermi surface and emphasized the role of the orbital matrix elements in determining the momentum structure of the gap. From their functional renormalization group calculations, they find that the degree of gap anisotropy depends upon the relative weight of the orbital matrix elements. They find that by tuning some of the tight-binding parameters to alter the relative orbital weights, one can change the anisotropy of the gap. Thomale *et al* [50] have also recently reported functional renormalization group results and argue that a nodal superconducting gap can appear on the β electron Fermi surfaces when the γ Fermi surface is absent.

Many authors have considered a Hamiltonian with all possible two-body on-site interactions between electrons in Fe orbitals as a good starting point for a microscopic

description of this system,

$$H = H_0 + \bar{U} \sum_{i,\ell} n_{i\ell\uparrow} n_{i\ell\downarrow} + \bar{U}' \sum_{i,\ell'<\ell} n_{i\ell} n_{i\ell'} + \bar{J} \sum_{i,\ell'<\ell} \sum_{\sigma,\sigma'} c^{\dagger}_{i\ell\sigma} c^{\dagger}_{i\ell'\sigma'} c_{i\ell\sigma'} c_{i\ell'\sigma} + \bar{J}' \sum_{i,\ell'\neq\ell} c^{\dagger}_{i\ell\uparrow} c^{\dagger}_{i\ell\downarrow} c_{i\ell'\downarrow} c_{i\ell'\uparrow}, \tag{1}$$

where $n_{i\ell} = n_{i,\ell\uparrow} + n_{i\ell\downarrow}$. The interaction parameters $\bar{U}$, $\bar{U}'$, $\bar{J}$ and $\bar{J}'$ correspond to the notation of Kuroki *et al* [3] and are related to those used by Graser *et al* [4] by $\bar{U} = U$, $\bar{J} = J/2$, $\bar{U}' = V + J/4$ and $\bar{J}' = J'$. The kinetic energy H_0 is described by a tight-binding model [4] spanned by the 5 Fe d orbitals, which, depending on the tight-binding parameters and the filling n, give rise to the Fermi surfaces shown in figure 1. Here in the 1 Fe per unit cell Brillouin zone that we will use, there are the usual α_1 and α_2 hole Fermi surfaces around the Γ point, the two β_1 and β_2 Fermi surfaces around $(\pi, 0)$ and $(0, \pi)$ and for the hole-doped case $n = 5.95$ shown in figure 1, there is an extra hole FS γ around the (π, π) point. We use a notation in which a given orbital index $\ell \in (1, 2, \ldots, 5)$ denotes the Fe-orbitals $(\mathrm{d}_{xz}, \mathrm{d}_{yz}, \mathrm{d}_{xy}, \mathrm{d}_{x^2-y^2}, \mathrm{d}_{3z^2-r^2})$. An important role will be played by the orbital matrix elements $a^{\ell}_{\nu}(\mathbf{k}) = \langle \ell | \nu \mathbf{k} \rangle$ which relate the orbital and band states. The dominant orbital weights $|a^{\ell}_{\nu}(\mathbf{k})|^2$ on the Fermi surfaces are illustrated in figure 1.

In equation (2), we have separated the intra- and inter-orbital Coulomb repulsion, as well as the Hund's rule exchange J and 'pair hopping' term J' for generality, but note that if they are generated from a single two-body term with SRI, they are related by $\bar{U}' = \bar{U} - 2\bar{J}$ and $\bar{J}' = \bar{J}$. Below we also consider the case where SRI is explicitly broken by other interactions in the crystal, such that $\bar{J}'$ and $\bar{U}'$ can take on independent values.

The analysis of individual orbital contributions to pair scattering can be a powerful tool to understand the influence of electronic structure on pairing. The basic picture that emerges from the spin fluctuation theories [3, 4] is straightforward. The intra-orbital scattering of d_{xz} and d_{yz} pairs between the α and β Fermi surfaces by $(\pi, 0)$ and $(0, \pi)$ spin fluctuations leads naturally to a gap that changes sign between the $\mathrm{d}_{xz}/\mathrm{d}_{yz}$ parts of the α Fermi surfaces/the d_{yz} and d_{xz} parts of the β_1 and β_2 electron pockets. However, intra-orbital scattering between the d_{xy} portions of the β_1 and β_2 Fermi surfaces suppresses the gap in the d_{xy} regions of the β Fermi surface and competes with the formation of an isotropic $\mathrm{s}^{\pm}$ gap. In addition, this anisotropy can also be driven by the need to reduce the effect of the on-site Coulomb interaction [41, 45]. There can also be inter-orbital pair scattering, such that for example a d_{xz} pair on α_1 scatters to a d_{xy} pair on β_1. These inter-orbital scattering processes that depend on $\bar{U}'$ and $\bar{J}'$ are weaker than the intra-orbital processes for SRI parameters where $\bar{U}' + \bar{J}' = \bar{U} - \bar{J}$ and $\bar{J}' = \bar{J}$. However, as noted by Zhang *et al* [51], the interaction parameters in the solid will be renormalized and one may have non-spin rotationally invariant (NSRI) interaction parameters leading to enhanced inter-orbital pairings.

Here, we explore these issues using the results obtained from a five-orbital RPA calculation to further examine the effects of the electronic structure, the doping and the interaction parameters on the structure of the gap. Analytical results for orbital components of the pairing vertices have allowed us to understand the factors that influence the structure of the gap, and in particular the transition from nodal to nodeless behavior. In section 2, we introduce the effective pair scattering vertex, its fluctuation-exchange RPA form and the pairing strength functional that determines the momentum dependence of the gap function [4]. Results for the gap function $g(\mathbf{k})$ obtained for a typical set of SRI interaction parameters are discussed in section 3. The strongest pairings occur in the A_{1g} channel and the discussion in this section focuses on the role

of doping and the presence of the γ pocket in determining whether the gap is nodeless. The nodeless character is found to be related to the additional resonant pairing provided by the γ sheet and is associated with the strong tendency for pairing between like orbitals when the γ pocket is of d_{xy} character. The origins of the tendency to pair in like orbitals are then explored in section 3. NSRI interaction parameters are discussed in section 4, where we examine the effect of the Hund's rule exchange $\bar{J}$ and the pair hopping $\bar{J}'$ on the pairing interaction and the nodal structure of the gap. Section 5 contains a further discussion of the effect of the orbital character of the γ hole pocket as well as the possible role of surface effects in causing nodeless behavior. Our conclusions are contained in section 7, and in appendix A we discuss some approximate forms for the pairing vertex.

2. Spin fluctuation pairing

As in [4], we analyze the effective pair scattering vertex $\Gamma(\mathbf{k}, \mathbf{k}')$ in the singlet channel,

$$\Gamma_{ij}(\mathbf{k}, \mathbf{k}') = \mathrm{Re}\left[\sum_{\ell_1\ell_2\ell_3\ell_4} a^{\ell_2,*}_{\nu_i}(\mathbf{k}) a^{\ell_3,*}_{\nu_i}(-\mathbf{k}) \Gamma_{\ell_1\ell_2\ell_3\ell_4}(\mathbf{k}, \mathbf{k}', \omega = 0) a^{\ell_1}_{\nu_j}(\mathbf{k}') a^{\ell_4}_{\nu_j}(-\mathbf{k}')\right], \tag{2}$$

where the momenta $\mathbf{k}$ and $\mathbf{k}'$ are restricted to the various Fermi surface sheets with $\mathbf{k} \in C_i$ and $\mathbf{k}' \in C_j$. The orbital vertex functions $\Gamma_{\ell_1\ell_2\ell_3\ell_4}$ represent the particle–particle scattering of electrons in orbitals ℓ_1, ℓ_4 into ℓ_2, ℓ_3 (see figure 2) and in the fluctuation exchange formulation [52, 53] are given by

$$\Gamma_{\ell_1\ell_2\ell_3\ell_4}(\mathbf{k}, \mathbf{k}', \omega) = \left[\tfrac{3}{2}\bar{U}^s \chi_1^{\mathrm{RPA}}(\mathbf{k} - \mathbf{k}', \omega)\bar{U}^s + \tfrac{1}{2}\bar{U}^s - \tfrac{1}{2}\bar{U}^c \chi_0^{\mathrm{RPA}}(\mathbf{k} - \mathbf{k}', \omega)\bar{U}^c + \tfrac{1}{2}\bar{U}^c\right]_{\ell_3\ell_4\ell_1\ell_2}, \tag{3}$$

where each of the quantities $\bar{U}^s$, $\bar{U}^c$, χ_1, etc represent matrices in orbital space as specified in appendix A. Note that the χ_1^{RPA} term describes the spin-fluctuation contribution and the χ_0^{RPA} term the orbital (charge)-fluctuation contribution.

For the parameter regions we will discuss, the dominant contribution to the pairing comes from the $S = 1$ particle–hole exchange given by the first term in equation (3). The forms of the interaction matrices $\bar{U}^s$ and $\bar{U}^c$ are given in appendix A. As illustrated in figure 2, there are intra-orbital, inter-orbital and mixed-orbital pair scattering processes. The contributions of each to the total pair scattering vertex Γ_{ij} in equation (3) are quite different. In particular, as discussed below, the orbital matrix elements for $\mathbf{k}$ and $-\mathbf{k}$ states on the Fermi surface favor pairs that are formed from electrons in the same orbital state. We therefore find that, although the mixed-orbital scattering can be significant, its contribution to the pairing interaction is negligible.

If one writes the superconducting gap $\Delta(\mathbf{k})$ as $\Delta g(\mathbf{k})$, with $g(\mathbf{k})$ being a dimensionless function describing the momentum dependence of the gaps on the Fermi surfaces, then $g(\mathbf{k})$ is determined as the stationary solution of the dimensionless pairing strength functional [4]

$$\lambda[g(\mathbf{k})] = -\frac{\sum_{ij} \oint_{C_i} \frac{\mathrm{d}k_\parallel}{v_{\mathrm{F}}(\mathbf{k})} \oint_{C_j} \frac{\mathrm{d}k'_\parallel}{v_{\mathrm{F}}(\mathbf{k}')} g(\mathbf{k}) \Gamma_{ij}(\mathbf{k}, \mathbf{k}') g(\mathbf{k}')}{(2\pi)^2 \sum_i \oint_{C_i} \frac{\mathrm{d}k_\parallel}{v_{\mathrm{F}}(\mathbf{k})} [g(\mathbf{k})]^2}, \tag{4}$$

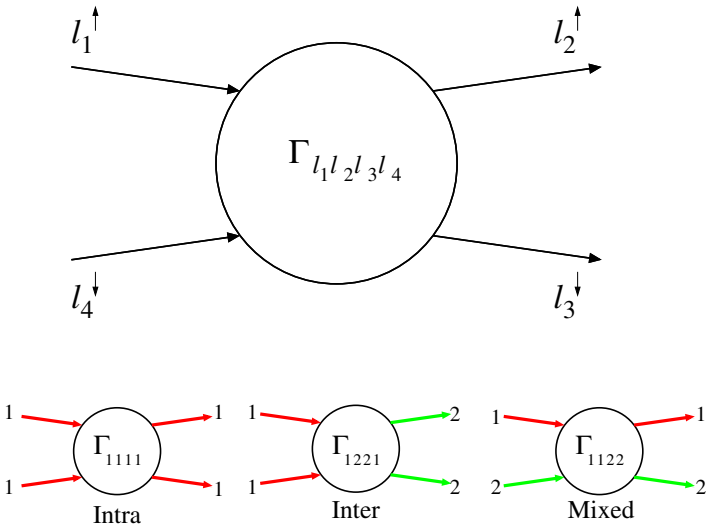

Figure 2. Top: the pairing vertex $\Gamma_{\ell_1\ell_2\ell_3\ell_4}$ defined in terms of orbital states ℓ_i of incoming and outgoing electrons. Bottom: representative examples of classes of orbital vertices referred to in the text: intra-, inter- and mixed-orbital vertices.

with the largest coupling strength λ. Here the momenta $\mathbf{k}$ and $\mathbf{k}'$ are restricted to the various Fermi surfaces $\mathbf{k} \in C_i$ and $\mathbf{k}' \in C_j$ and $v_{\mathrm{F},\nu}(\mathbf{k}) = |\nabla_{\mathbf{k}} E_\nu(\mathbf{k})|$ is the Fermi velocity on a given Fermi surface. The eigenvalue λ provides a dimensionless measure of the pairing strength.

3. The spin-rotational invariance (SRI) case

Below we discuss the essential physics of the gapped-nodal transition within the constrained interaction parameter subspace where SRI is assumed. It is worth recalling the main points of the argument for an isotropic $s^{\pm}$ state: (i) that a repulsive effective interaction peaked near $(\pi, 0)$ would drive such a state provided (ii) this interaction did not vary significantly over the small Fermi surface pockets [14]. Our main points are as follows.

- The largest pair scattering processes tending to stabilize an isotropic $s^{\pm}$ state are the intra-orbital scattering pairing vertices Γ_{aaaa} (cf figure 2), which are peaked near $(\pi, 0)$.
- The intra-orbital processes primarily affect the gap on the sections of the Fermi surface with the corresponding orbital character. The relative signs between various orbital sections are determined by subdominant intra- and inter-orbital processes.
- The isotropic $s^{\pm}$ state can be frustrated by intraband Coulomb scattering and by pair scattering processes between the two electron sheets with $\mathbf{q} \sim (\pi, \pi)$, both of which favor nodes [41].
- The γ pocket of d_{xy} character can overcome this frustration and stabilize the nodeless state [42].
- If the Hund's rule coupling $\bar{J}$ is weak, the processes induced by the γ pocket are not sufficient to eliminate the nodes. The Hund's rule exchange is necessary to overcome an

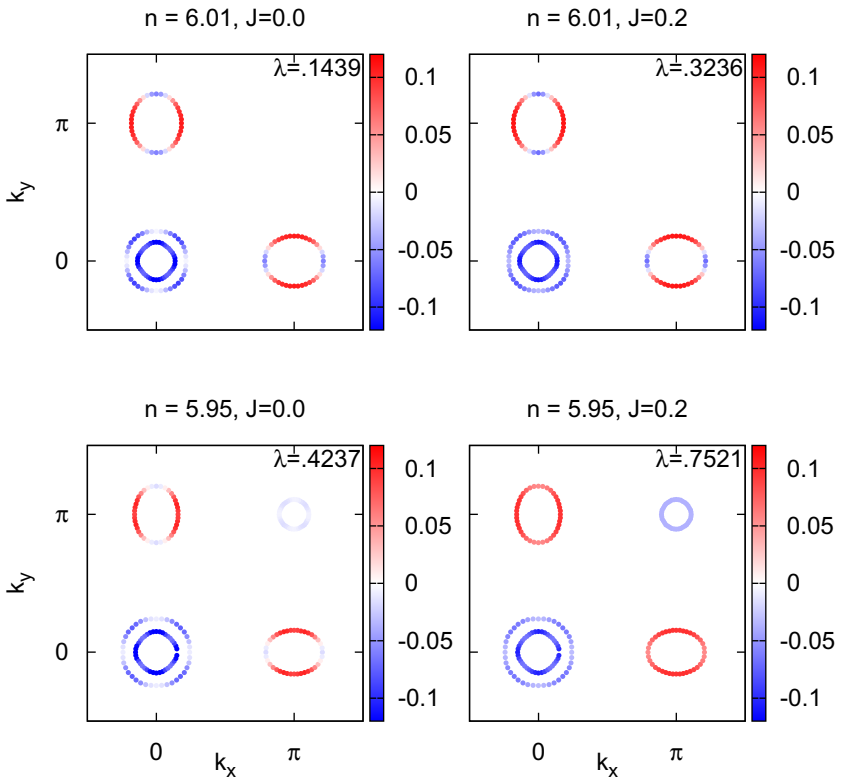

Figure 3. The gap eigenfunctions $g(k)$ for a spin rotationally invariant parameter set $\bar{U} = 1.3$, $\bar{J} = 0.0$ and 0.2, for dopings $n = 5.95$ (bottom) and $n = 6.01$ (top).

attractive $(\pi, 0)$ interaction between d_{xz} (d_{yz}) pairs and d_{xy} pairs and drive a strong intra-orbital d_{xz} and d_{yz} repulsion.

To illustrate these points, we begin by plotting gap functions $g(\mathbf{k})$ for two typical sets of SRI interaction parameters $\bar{U} = 1.3$, $\bar{J} = 0.0$ and 0.2 and two different fillings $n = 6.01$ and 5.95, as shown in figure 3. In the electron-doped case ($n = 6.01$), the γ Fermi surface around (π, π) is absent and one finds an anisotropic gap with nodes on the β_1 and β_2 Fermi surfaces for zero and for finite $\bar{J}$ [4]. The doping dependence at fixed $\bar{J}$ of the gap $g(\mathbf{k})$ versus angle around the β_1 Fermi surface is shown in figure 4. The nodes arise in part because of the β_1–β_2 pair scattering and other aspects of the interactions which frustrate the isotropic $s^{\pm}$ state [21]. In particular, the sign change of the gaps on the end regions of the β Fermi surfaces reduces some of the frustration which arises from the $\beta_1 - \beta_2$ scattering [42]. In addition, this sign change acts to suppress the effect of the intra-band Coulomb repulsion.

For the hole-doped case ($n = 5.95$) and finite $\bar{J}$, the gap function, as seen in figures 3 and 4, is anisotropic but nodeless. As discussed in [42], the scattering between the γ (π, π) Fermi surface and the β_1 and β_2 Fermi surfaces stabilizes the nodeless gap. While there is still frustration associated with the β_1–β_2 pair scattering, the additional β_1–γ and β_2–γ pair scattering processes overcome it. The presence of the pocket also increases the overall pairing strength, which can be seen by comparing the pairing eigenvalues in the figure; this would correspond to an increase in the critical temperature. To see how these effects arise in more detail, in figure 5 we have plotted several of the orbital pairing vertices $\Gamma_{\ell_1\ell_2\ell_3\ell_4}(\mathbf{q})$ for $\mathbf{q}$ along

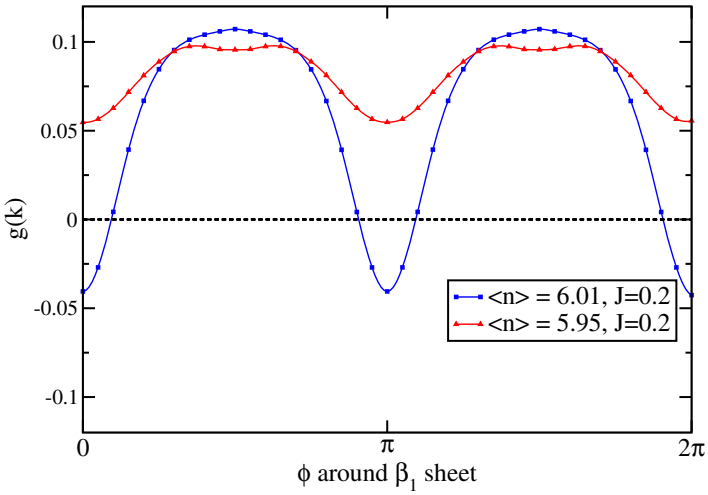

Figure 4. The gap function $g(k)$ on the β_1 pocket for $n = 5.95$, $\bar{J} = 0.2$ (red triangles) and $n = 6.01$, $\bar{J} = 0.2$ (blue squares). Here the angle ϕ is measured from the k_x-axis.

high symmetry directions in the Brillouin zone for both $n = 5.95$ and 6.01. The peak in $\Gamma_{2222}(\mathbf{q})$ near the X point arises from $\mathbf{q} = (\pi, 0)$ scattering processes in which d_{yz} pairs are scattered between the α and β_1 Fermi surfaces. In the presence of the γ sheet, both $\Gamma_{3333}(\mathbf{q})$ intra-orbital d_{xy} pair scattering between $\beta_{1,2}$ and γ as well as $\Gamma_{1331}(\mathbf{q})$ and $\Gamma_{2332}(\mathbf{q})$ inter-orbital d_{xz}, d_{yz} pair to d_{xy} pair scattering between $\beta_{1,2}$ and γ are also possible. The pair scattering from the β sheets to the γ hole pocket, represented by Γ_{3333}, provides a strong resonant stabilization of the nodeless state; we have verified that the nodal behavior is recovered when it is neglected. As discussed previously, although mixed-orbital vertices such as Γ_{2233} are present, their contribution to $\Gamma_{ij}(\mathbf{k}, \mathbf{k}')$ is suppressed by the orbital matrix elements in equation (3), and the pairing is dominated by intra- and inter-orbital scattering.

To further illustrate this, in figure 6 we have plotted the pairing interaction $\Gamma_{ij}(\mathbf{k}, \mathbf{k}')$ that determines the gap via equation (4). In these plots, one member of a $(\mathbf{k}', -\mathbf{k}')$ pair is located at the wave vector denoted by a black circle in the figure. The plot shows the strength of the pairing interaction $\Gamma_{ij}(\mathbf{k}, \mathbf{k}')$ associated with the scattering of this $(\mathbf{k}', -\mathbf{k}')$ pair to a $(\mathbf{k}, -\mathbf{k})$ pair on the various Fermi surfaces. One sees that if the initial pair is located in a region that has predominantly d_{xz}-orbital character (top), the strongest scattering is to a pair $(\mathbf{k}, -\mathbf{k})$ on other d_{xz} regions [21]. Similarly, there are strong d_{yz} intra-orbital scattering processes that are obtained by rotating the figures by $\pi/2$. While inter-orbital scattering processes are also present, they are weaker for the parameters we have considered here, as seen, e.g., from the plot of Γ_{2332} in figure 5. In addition to the d_{yz} intra-orbital scattering, there is strong d_{xy} intra-orbital scattering between β_2 and γ as well as between β_1 and γ. Note that in figure 6 the pairing strength is anisotropic along the Fermi sheets, violating one of the key assumptions underlying the argument for an isotropic $s^{\pm}$ state.

We return to the role of the Hund's rule exchange $\bar{J}$ in stabilizing a nodeless state. The main effect, i.e. the lifting of the nodes as $\bar{J}$ is turned on, is illustrated in figure 7. There are two reasons this occurs. Firstly, as discussed in appendix A, the intra-orbital Γs are controlled by $\bar{U}$ and $\bar{J}$ (see equations (A.7) and (A.8)). For a fixed $\bar{U}$, increasing $\bar{J}$ drives the system closer to the

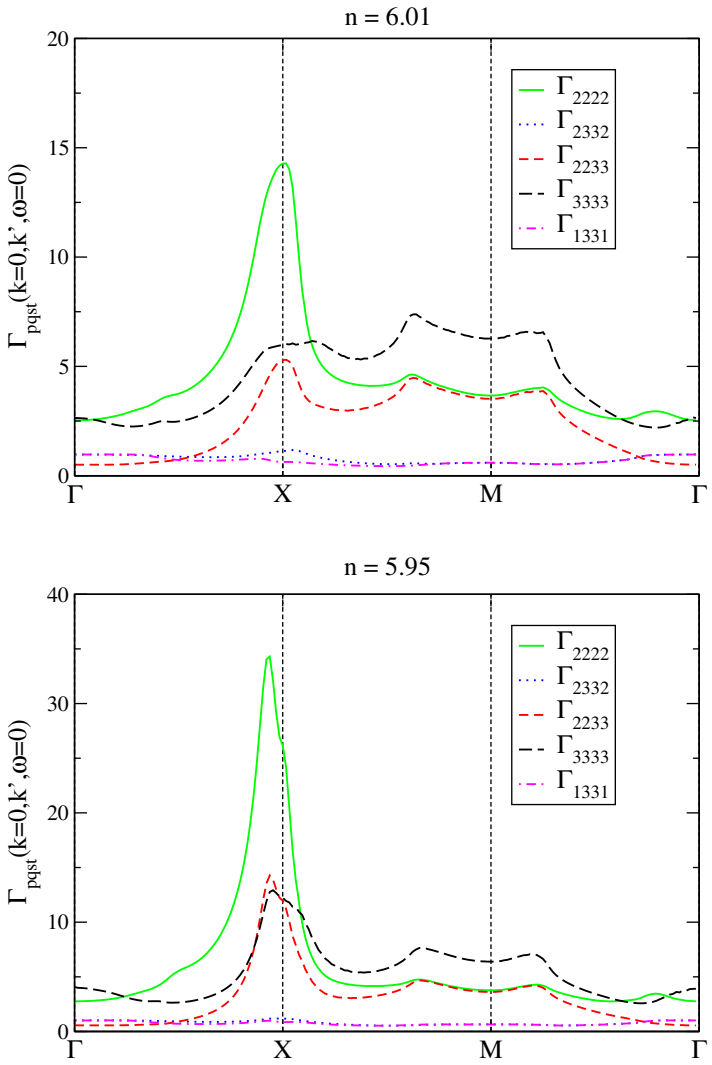

Figure 5. Orbital pairing vertices along high symmetry directions in q space for $\bar{U} = 1.3$, and $\bar{J} = 0.2$ for $n = 5.95$ (bottom) and $n = 6.01$ (top), spin rotation invariance assumed. Solid (green) line: Γ_{2222} (intra); dotted (blue) Γ_{2332} (inter); dashed (red) Γ_{2233} (mixed); dashed (black) Γ_{3333}; dash-dotted (magenta) Γ_{1331} (inter). Note that the vertical scales in the two panels are different.

instability and thus enhances the leading peak in the RPA susceptibility. However, equation (3) also contains the term $\frac{1}{2}(\bar{U}^s + \bar{U}^c)$, which involves only the bare interactions rather than the RPA-enhanced susceptibilities. This term contributes to the intra-band Coulomb interaction (which favors anisotropic pairing on the electron sheets) and scales, in the dominant orbital channels, with $\bar{U}$ rather than $\bar{J}$. Thus increasing $\bar{J}$ increases the importance of the χ_1^{RPA} term in equation (3) relative to the intraband Coulomb interaction favoring the isotropic state.

Secondly, we find that inter-orbital d_{xy} to d_{xz} pair scattering, represented by Γ_{1331}, plays an important role in stabilizing the isotropic state when a Hund's rule exchange is present. If $\bar{J} = 0$, figure 8 shows that the pair scattering has an attractive peak at $(\pi, 0)$, which tends to induce nodes on the β Fermi surface. If $\bar{J} > 0$, on the other hand, this attractive peak changes

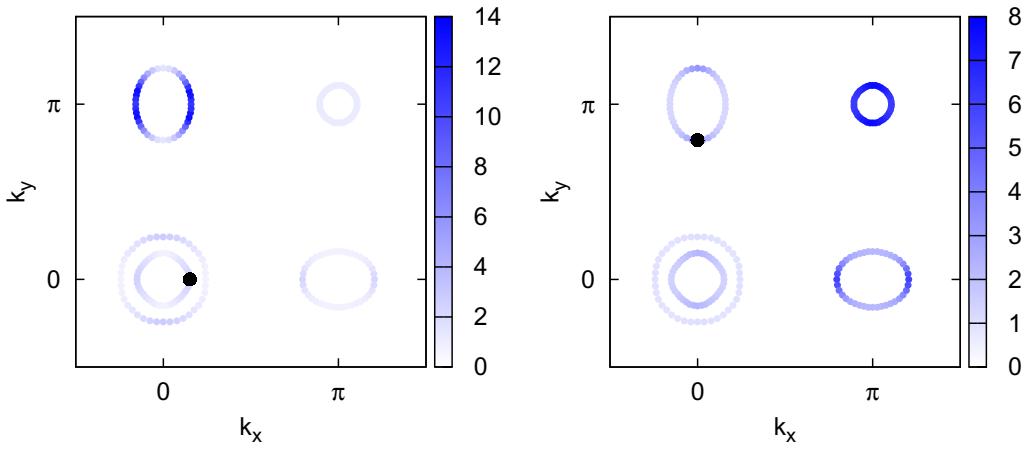

Figure 6. The total pair scattering vertex $-\Gamma_{ij}(k, k')$ for $n = 5.95$ with parameters $\bar{U} = 1.3$ and $\bar{J} = 0.2$ as a function of k with k' set to the point on the Fermi surface indicated in each panel by the black dot.

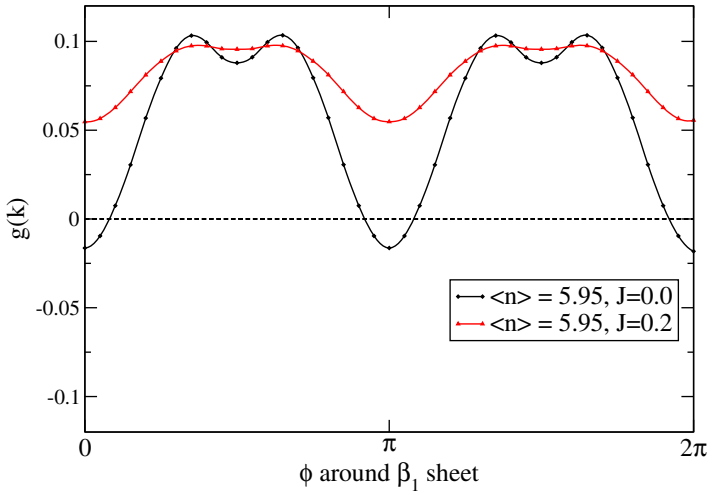

Figure 7. The gap function $g(k)$ on the β_1 pocket for $n = 5.95$, $\bar{J} = 0$ (black diamonds) and $n = 5.95$, $\bar{J} = 0.2$ (red triangles). Here the angle ϕ is measured from the k_x-axis.

sign, as discussed in section 4 and in appendix A, and a nodeless state is stabilized by the dominant intra-orbital pairing vertices.

Finally, we note that in Graser *et al* [4], upon electron doping, a d-wave solution overtakes the anisotropic s-wave one. Here, we find that upon strong hole doping (∼8%), the spin-fluctuation approximation also leads to a d-wave solution.

4. Broken SRI

In leading order, the strength of the inter-orbital pair scattering is determined by U' and J'. For SRI parameters $\bar{U}' = \bar{U} - \bar{J} - \bar{J}'$, the intra-orbital pair scattering tends to dominate the pairing

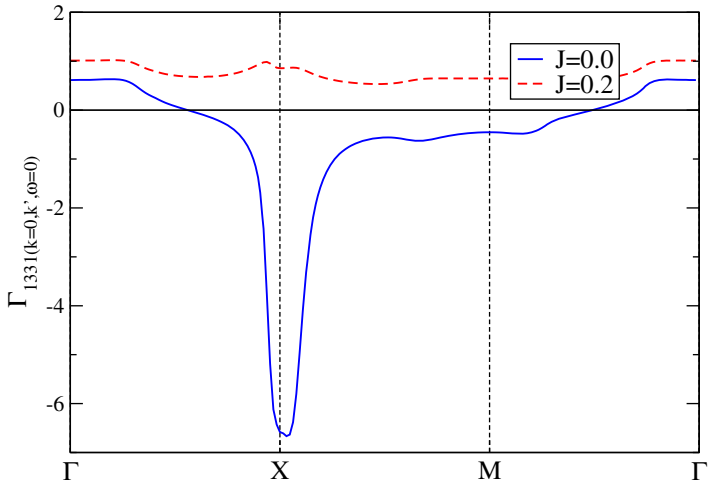

Figure 8. The inter-orbital pair scattering vertex $\Gamma_{1331}(\mathbf{q})$ along high symmetry directions for $n = 5.95$ with parameters $\bar{U} = 1.3$ and $\bar{J} = 0.0, 0.2$.

interaction as we have seen in the previous section. However, as noted by Zhang *et al* [51], the actual interaction parameters appropriate for the Fe-superconducting materials need not be SRI. In this case, inter-orbital pair scattering may play a more important role in determining the momentum dependence of the gap function $g(\mathbf{k})$. In addition, using non-SRI parameters, we can separately explore the roles of the exchange coupling $\bar{J}$ and the pair hopping $\bar{J}'$ interactions on the structure of the pairing interactions and the gap. Here, for a filling $n = 5.95$, we hold $\bar{U}$ and $\bar{U}'$ fixed and examine the roles of $\bar{J}$ and $\bar{J}'$ on the nodal-gapped transition on the β_1 pockets near $(\pi, 0)$. The discussion below applies also to the β_2 pocket near $(0, \pi)$ with orbital states rotated by 90°.

In figure 9, we plot both the various relevant orbital pairing vertices along high symmetry directions in momentum space as well as the leading gap function $g(\mathbf{k})$ on the β_1 sheet. Beginning with the nodal case $\bar{J} = \bar{J}' = 0$, we can see that increasing $\bar{J}$ only weakly affects the momentum space structure of the gap. However, note that the $g(\mathbf{k})$ plotted in figure 9 is normalized and should be scaled by the corresponding eigenvalue λ to obtain the true gap amplitude. Turning on $\bar{J}$ indeed increases the pairing eigenvalue λ by causing an overall increase in the pairing vertices. The largest scattering is provided by Γ_{2222} near $(\pi, 0)$, which is driven up by increasing $\bar{J}$; this can be understood by observing that the RPA-renormalized susceptibility is enhanced by increasing $\bar{J}$ (see equation (A.7)). This clearly enhances the strength of the gap on the parts of the β_1 Fermi surface characterized by a strong d_{yz} orbital content. And, as discussed above, the repulsive nature of the interaction forces the gap on the d_{yz} sections of the β_1 sheet to have the opposite sign of the gap on the d_{yz} sections of the α_1 and α_2 sheets. This also applies to the Γ_{1111} vertex and corresponding d_{xz} sections of the Fermi surface. The gap on the remaining portions of the Fermi surface, which are of d_{xy} character, are left to be determined by the largest other pair scattering with a d_{xy} component, which for these parameters is Γ_{1331}. As discussed in appendix A, the Hund's rule coupling $\bar{J}$ contributes to an increase in the intra-orbital repulsive scattering, which favors a nodeless gap, while also (see equation (A.10)) leading to a more negative Γ_{1331} scattering, which favors a nodal gap. The net result, as seen in figure 9(b), is that the nodes remain for $\bar{J} = 0.1$ and $\bar{J}' = 0$. Alternatively, for the case in which $\bar{J}' = 0.1$ and $\bar{J} = 0$, as shown in figure 9(c), the nodes are 'lifted'. In this case, $\bar{J}'$ is sufficient

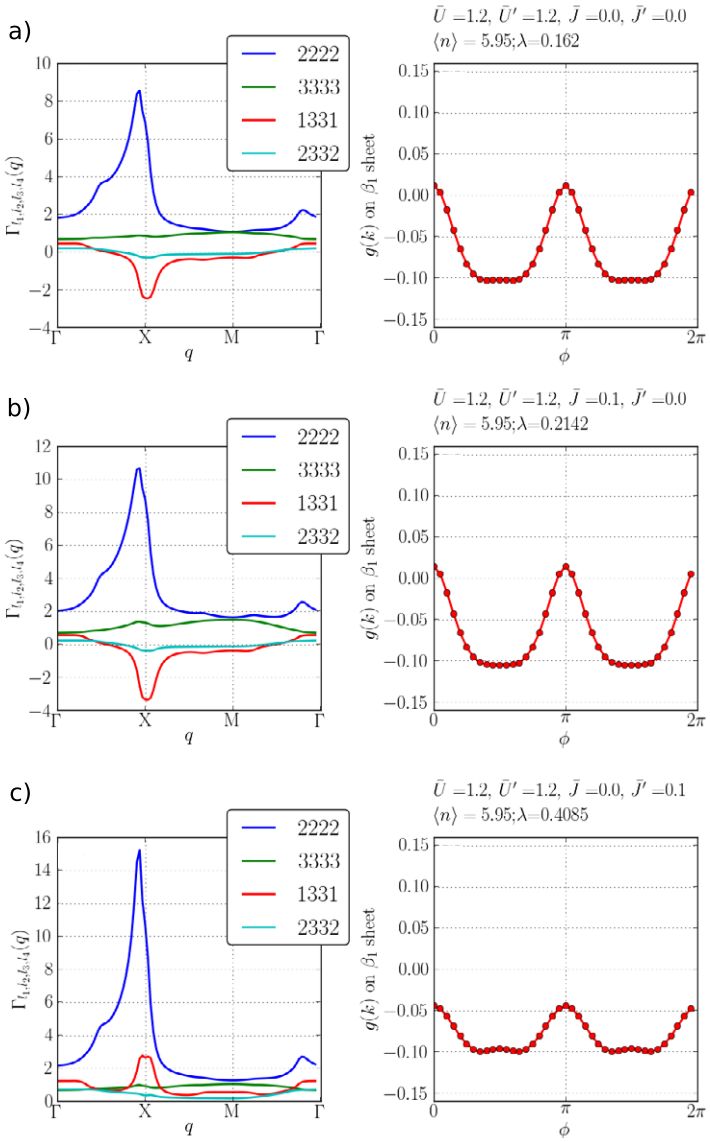

Figure 9. Left: orbital pairing vertices, and right: gap function on the β_1 sheet, for $\bar{U} = 1.2$, $\bar{U}' = 1.2$ and $n = 5.95$. Cases shown are $\bar{J} = \bar{J}' = 0$ ((a), $\lambda = 0.10$); $\bar{J} = 0.1$, $\bar{J}' = 0$ ((b), $\lambda = 0.21$); $\bar{J} = 0$, $\bar{J}' = 0.1$ ((c), $\lambda = 0.41$).

to overcome the negative contribution of $\bar{U}'^2\chi^0_{1331}$. Here, Γ_{1331} has changed sign due to the contribution of equation (A.9), which is stronger than the contribution of $\bar{U}'$ (equation (A.10)) due to its resonant structure. The change in sign now favors the same sign across the whole β sheet, which causes the nodes to lift.

5. The orbital character of the hole pocket

We have discussed the appearance of the γ hole pocket with doping in the context of doping by a rigid band shift of the 1111 Fermi surface of Cao *et al* [7]. There appear to be various other scenarios in which electronic structure distortions might occur. For example, as noted by Kuroki

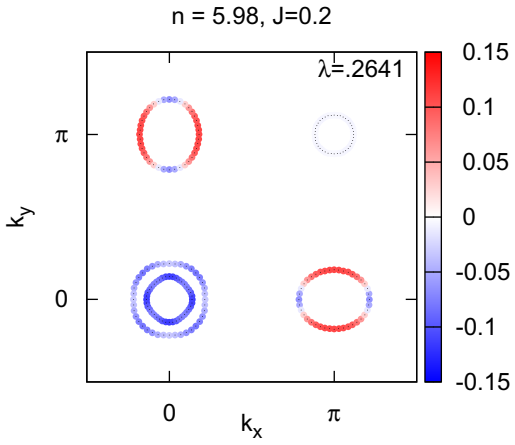

Figure 10. The eigenfunction for the hole-doped (x = 2%) compound where the pocket character has been adjusted to be of $d_{3z^2-r^2}$ type. The interaction parameters have been chosen as $\bar{U} = 1.3$, $\bar{J} = 0.2$.

et al [42], variations in the As height, which are known to occur in the 1111 family, can tune the size of the γ pocket and thereby the pairing itself, independent of doping. Another effect of the As height noted by Calderón *et al* [44] is a switching of two bands near Γ such that the γ pocket that occurs upon hole doping is of primarily $d_{3z^2-r^2}$ character rather than d_{xy}. Within our framework, we can imitate this effect simply by adjusting the size of certain tight-binding coefficients associated with the Fe–As hopping in order to create such a $d_{3z^2-r^2}$ pocket at γ, and ask what effect this has on the pairing. As also found by Calderón *et al*, the new γ pocket that appears is the only Fermi surface sheet with $d_{3z^2-r^2}$ character, so one may expect the pairing to be substantially altered relative to the situation with a γ pocket of d_{xy} character. In figure 10, we see that when the electronic structure is adjusted to create a $d_{3z^2-r^2}$ pocket instead of a d_{xy}, the pairing eigenfunction reverts to the nodal s-type found in the electron-doped case, as expected since the additional γ–β condensation energy that stabilized the isotropic state has been lost. In addition, the pairing strength λ is substantially reduced.

6. The effect of surface on pair state

As noted above, the presence of a hole pocket of mainly d_{xy} character around (π, π) in the unfolded zone causes a nodeless state to be favored over a nodal one (cf figure 3). As pointed out by Kuroki *et al* [3], this can be accomplished by an increase of the pnictogen height h_{Pn}. To provide some additional insight into the emergence of nodeless behavior, in particular in ARPES experiments [8]–[13], we have performed first-principles calculations on a slab of $BaFe_2As_2$ containing six FeAs layers.

The calculations were performed using the Quantum-ESPRESSO package [54], which uses a plane wave basis. We used the Perdew–Burke–Ernzerhof [55] exchange-correlation functionals and ultrasoft pseudopotentials. The use of ultrasoft pseudopotentials enabled us to utilize an energy cut-off of 40 Ryd for the plane wave basis, while the density cut-off was taken to be 400 Ryd. To determine the positions of the surface ions, two layers in the middle were kept fixed, and the rest of the atoms were allowed to relax. We find that the pnictogen height near the surface and the c-axis lattice constant contract, by about 13 and 5%, respectively.

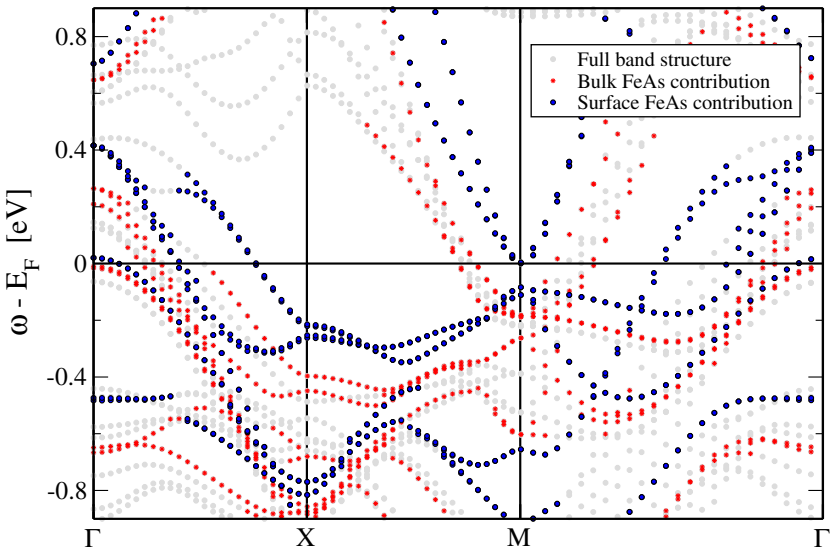

Figure 11. The DFT band structure calculated for a $BaFe_2As_2$ slab (gray points). The red points show the bulk contributions from the FeAs layers, while the black points denote the corresponding surface contributions.

Figure 11 shows the band structure obtained for the $BaFe_2As_2$ slab. To determine the origin of the bands, we projected the band structure on the atomic wavefunctions of the ions. A particular ϵ_k is considered to belong to a certain ion if the projection onto the atom is larger than 50%. We have verified that the results below do not change appreciably if the projection threshold is varied.

As can be seen from the figure, the presence of the surface causes the band just below the Fermi energy in the bulk to rise slightly, causing the appearance of an additional Fermi surface. Note that these results are in the folded zone; zone folding causes the pocket at (π, π) to appear at Γ, and it is this pocket that is seen due to the surface. For this pocket to cause a nodeless gap, it is necessary that it is of d_{xy} character (or $d_{x^2-y^2}$ in the folded zone), which we have confirmed (not shown). Thus, it is possible that due to the sensitive nature of the band structure, the (necessary) presence of a surface can cause surface probes to detect a nodeless gap, even when the bulk gap has nodes.

7. Conclusions

One of the striking features of Fe superconductors is the sensitivity of the momentum space structure of the superconducting gap to relatively small changes in the electronic structure. Indeed, the electronic structure of these materials is quite special. Firstly, they are semi-metallic with multiple, nearly compensated electron and hole Fermi surfaces. Secondly, multiple Fe orbitals lie near the Fermi energy. This means that relatively small changes in the doping or atomic structure can alter the nesting, the orbital composition of the band states on the Fermi surface and even the number of $k_z = 0$ Fermi surfaces. The most prominent example of this phenomenon is the appearance of the so-called (π, π) hole pocket, studied first by Kuroki *et al*, with hole doping or pnictogen height [42].

Within the framework of an RPA fluctuation exchange approximation, we can understand how these changes affect the structure of the superconducting gap. For the parameter regime that we have studied, the leading pairing state has A_{1g} symmetry. It is basically an $s^{\pm}$ state, but the anisotropy of the gap, and particularly the presence or absence of gap nodes on the electron Fermi surface sheets is sensitive to the electronic structure. It is important to note that this type of unconventional nodal state is much more sensitive than, for example, the $d_{x^2-y^2}$ pair state of the cuprates, where nodes owe their existence to symmetry; instead, in the Fe-pnictides the nodes appear to be 'accidental', i.e. determined by details of the pair interaction.

As discussed in earlier works, the dominant pairing processes involve intra-orbital scattering. In this case, the intra-orbital $(\pi, 0)$ and $(0, \pi)$ scattering processes lead to a change of sign between the regions on the α and β Fermi surfaces where the d_{xz} and d_{yz} orbital weights are dominant. However, β_1 to β_2 intra-orbital d_{xy} scattering tends to frustrate the isotropic $s^{\pm}$ state. Furthermore, the effect of the intraband Coulomb interaction can be reduced in an anisotropic state. Thus, for light electron doping ($n = 6.01$), where there are only the α and β Fermi surfaces, we find that the gap has nodes on the β sheets. This anisotropy is further enhanced by the inter-orbital scattering of d_{xz} (d_{yz}) pairs on α_1 (α_2) to d_{xy} pairs on the β sheets.

In the hole-doped case ($n = 5.95$), or if the band structure is adjusted, a hole pocket appears around the (π, π) point. For our band structure, this γ pocket has d_{xy} character. Intra-orbital d_{xy} scattering between the β and γ pockets favors a more isotropic gap, removing the nodes on the β Fermi surfaces. We note that if the band parameters were such that the orbital character of the γ Fermi surface were, for example, $d_{3z^2-r^2}$ instead of d_{xy}, the gap nodes would return to the β Fermi surfaces. In addition, the pairing strength λ is substantially reduced, reflecting the important role played by the orbital weights on the Fermi surface [56]. This illustrates the important role played by the orbital weight.

We also pointed out that various effects in addition to the pnictogen height identified as a key factor by Kuroki *et al* can influence the γ pocket. In particular, the presence of a surface can create such a pocket in a nominally electron-doped system, stabilizing a nodeless state. This may explain why ARPES experiments have reported quasi-isotropic gaps in these systems.

We have investigated in some detail the way in which the various single-site interaction parameters $\bar{U}$, $\bar{U}'$, $\bar{J}$ and $\bar{J}'$ influence the different types of pair scattering processes. The RPA technique is crude, but it allows analytical insights into questions of this type. We have therefore, been able to trace the effects of varying these parameters on the strength of the relevant orbital pair scattering vertices at appropriate nesting vectors, which in turn determines not only the overall magnitude of the pairing strength (i.e. T_c), but also the anisotropy of the gap on the Fermi surface. It is to be hoped that the influence of various changes in crystal structure, morphology, etc on the pair state and transition temperature may now be better understood through this type of analysis.

Acknowledgments

The authors acknowledge B A Bernevig, J Hu, A Chubukov, I Mazin, F Wang, R Thomale and H Ikeda for helpful comments and discussions. This work was supported by DOE DE-FG02-05ER46236 (PJH and AK) and by DOE/BES DE-FG02-02ER45995 (HPC and AK). SG acknowledges support from the DFG through SFB 484 and TRR 80, and DJS and TAM acknowledge the Center for Nanophase Materials Sciences, which is sponsored at Oak Ridge National Laboratory by the Division of Scientific User Facilities, US Department of Energy.

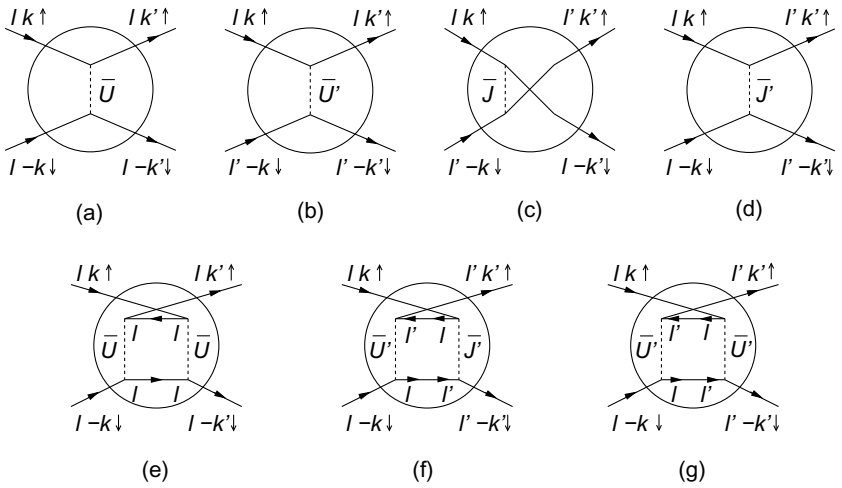

Figure A.1. The first-order (a–d) and some second-order (e–g) scattering vertices corresponding to intra- (a, e), inter- (d, f) and mixed-orbital (b, c, g) scattering processes.

Appendix A. The scattering vertices

The basic scattering vertices for the multiorbital Hubbard model are shown in figures A.1. Here, as noted in the introduction, we use a notation in which an orbital index $l = (1, 2, \ldots, 5)$ denotes the Fe-d orbitals (d_{xz}, d_{yz}, d_{xy}, $d_{x^2-y^2}$, $d_{3z^2-r^2}$). As seen, in lowest order, there are intra-orbital (a), inter-orbital (d) and mixed-orbital ((b) and (c)) pair scattering processes. Some second-order contributions are shown in figures A.1(e)–(g). The orbital matrix elements for $\mathbf{k}$ and $-\mathbf{k}$ states on the Fermi surface favor pairs that are formed from electrons in the same orbital state. Thus, although the mixed-orbital scattering can be significant, its contribution to the pairing interaction is negligible and the intra- and inter-orbital scattering processes give rise to the superconducting pairing [51]. The relative l-orbital contribution to the Bloch state $\mathbf{k}$ on the ν^{th} Fermi surface is given by the square of the orbital matrix element $|a_\nu^l(\mathbf{k})|^2$. As shown in figure 1, the $l = 1$ (d_{xz}) and $l = 2$ (d_{yz}) orbitals give the main contributions on the α Fermi surfaces. Likewise the $l = 1$ and $l = 3$ (d_{xy}) orbitals contribute to the β_2 Fermi surface, while the $l = 2$ and $l = 3$ orbitals contribute to the β_1 Fermi surface. For our tight-binding fit of the Cao *et al* band structure [7], the γ Fermi surface (around $M = (\pi, \pi)$) has predominantly $l = 3$ (d_{xy}) weight. The orbital weight distribution favors ($\mathbf{k}$, $-\mathbf{k}$) pairs with similar orbitals so that both, intra-orbital $(d_{xz}, d_{xz})_\alpha \leftrightarrow (d_{xz}, d_{xz})_{\beta_2}$, $(d_{yz}, d_{yz})_\alpha \leftrightarrow (d_{yz}, d_{yz})_{\beta_1}$ and inter-orbital $(d_{xz}, d_{xz})_\alpha \leftrightarrow (d_{xy}, d_{xy})_{\beta_2}$ and $(d_{yz}, d_{yz})_\alpha \leftrightarrow (d_{xy}, d_{xy})_{\beta_2}$ pair scattering processes, contribute. In addition, when the γ Fermi surface around (π, π) is present, there are important intra-orbital $(d_{xy}, d_{xy})_\gamma \leftrightarrow (d_{xy}, d_{xy})_{\beta_1}$ and $(d_{xy}, d_{xy})_\gamma \leftrightarrow (d_{xy}, d_{xy})_{\beta_2}$ pair scatterings. From figure A.1, one can see that the first-order intra-orbital scattering processes involve $\bar{U}$ and $\bar{J}$, while the inter-orbital processes depend on $\bar{U}'$ and $\bar{J}'$.

In the RPA fluctuation-exchange approximation, for the parameter range of interest, the dominant pairing interaction is given by equation (3) with

$$\chi_1^{\text{RPA}}(\mathbf{q}) = \chi^0(\mathbf{q})\left[1 - U^s\chi^0(\mathbf{q})\right]^{-1} \tag{A.1}$$

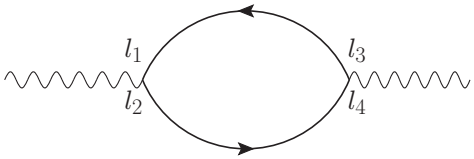

Figure A.2. Non-interacting susceptibility $\chi^0_{\ell_1,\ell_2,\ell_3,\ell_4}$ defined in terms of orbital states ℓ_i of incoming and outgoing electrons.

and

$$\chi_0^{\mathrm{RPA}}(\mathbf{q}) = \chi^0(\mathbf{q})\left[1 + U^c\chi^0(\mathbf{q})\right]^{-1}. \tag{A.2}$$

For the five-orbital problem, U^s, U^c and χ^0 are 25×25 matrices in an $(\ell_1\ell_2)$ basis with

$$U^s_{\ell_1\ell_2\ell_3\ell_4} = \begin{cases} \bar{U} & \ell_1=\ell_2=\ell_3=\ell_4, \\ \bar{U}', & \ell_1=\ell_3\neq\ell_2=\ell_4, \\ \bar{J} & \ell_1=\ell_2\neq\ell_3=\ell_4, \\ \bar{J}', & \ell_1=\ell_4\neq\ell_2=\ell_3, \end{cases} \tag{A.3}$$

$$U^c_{\ell_1\ell_2\ell_3\ell_4} = \begin{cases} \bar{U}, & \ell_1=\ell_2=\ell_3=\ell_4, \\ -\bar{U}'+2\bar{J}, & \ell_1=\ell_3\neq\ell_2=\ell_4, \\ 2\bar{U}'-\bar{J}, & \ell_1=\ell_2\neq\ell_3=\ell_4, \\ \bar{J}', & \ell_1=\ell_4\neq\ell_2=\ell_3. \end{cases} \tag{A.4}$$

and

$$\chi^0_{\ell_1\ell_2\ell_3\ell_4}(\mathbf{q}) = -\frac{1}{N}\sum_{\mathbf{k},\mu\nu}\frac{a^{\ell_4}_\mu(\mathbf{k})a^{\ell_2*}_\mu(\mathbf{k})a^{\ell_1}_\nu(\mathbf{k}+\mathbf{q})a^{\ell_3*}_\nu(\mathbf{k}+\mathbf{q})}{E_\nu(\mathbf{k}+\mathbf{q})-E_\mu(\mathbf{k})}\left[f(E_\nu(\mathbf{k}+\mathbf{q}))-f(E_\mu(\mathbf{k}))\right]. \tag{A.5}$$

Here μ and ν are summed over the band indices and f is the usual Fermi function. We have typically taken the temperature $T = 0.02\,\mathrm{eV}$. The orbital indexing convention for the susceptibility is illustrated in figure A.2.

As seen in figure 1, three orbitals 1 (d_{xz}), 2 (d_{yz}) and 3 (d_{xy}) have significant weight on the Fermi surfaces. Therefore, in this case, the interaction matrix U^s reduces to the 9×9 matrix shown in table A.1. Furthermore, as seen in figure A.3, the bare off-diagonal elements of the susceptibility involve single-particle propagators projected on different orbitals, which makes them smaller than the diagonal elements.

Keeping only the diagonal terms in χ_0, it is straightforward to evaluate the RPA susceptibility matrix. For example,

$$\begin{pmatrix} \chi_{1313} & \chi_{1331} \\ \chi_{3113} & \chi_{3131} \end{pmatrix}^{\mathrm{RPA}} = \begin{pmatrix} \chi^0_{1313} & 0 \\ 0 & \chi^0_{3131} \end{pmatrix}\begin{pmatrix} 1-\bar{U}'\chi^0_{1313} & -\bar{J}'\chi^0_{1313} \\ -\bar{J}'\chi^0_{3131} & 1-\bar{U}'\chi^0_{3131} \end{pmatrix}^{-1} \tag{A.6}$$

Using the fact that $\chi^0_{1313} = \chi^0_{3131}$ and setting $\chi^0_{1313} = \chi^0_{13}$, we have

$$\chi^{\mathrm{RPA}}_{1313} = \frac{1}{2}\chi^0_{13}\left(\frac{1}{1-(\bar{U}'+\bar{J}')\chi^0_{13}}+\frac{1}{1-(\bar{U}'-\bar{J}')\chi^0_{13}}\right)$$

$$\chi^{\mathrm{RPA}}_{1331} = \frac{1}{2}\chi^0_{13}\left(\frac{1}{1-(\bar{U}'+\bar{J}')\chi^0_{13}}-\frac{1}{1-(\bar{U}'-\bar{J}')\chi^0_{13}}\right),$$

Table A.1. Interaction matrix U^s in the reduced 1 (d_{xz}), 2 (d_{yz}) and 3 (d_{xy}) basis.

	11	22	33	12	21	13	31	23	32
11	$\bar{U}$	$\bar{J}$	$\bar{J}$						
22	$\bar{J}$	$\bar{U}$	$\bar{J}$						
33	$\bar{J}$	$\bar{J}$	$\bar{U}$						
12				$\bar{U}'$	$\bar{J}'$				
21				$\bar{J}'$	$\bar{U}'$				
13						$\bar{U}'$	$\bar{J}'$		
31						$\bar{J}'$	$\bar{U}'$		
23								$\bar{U}'$	$\bar{J}'$
32								$\bar{J}'$	$\bar{U}'$

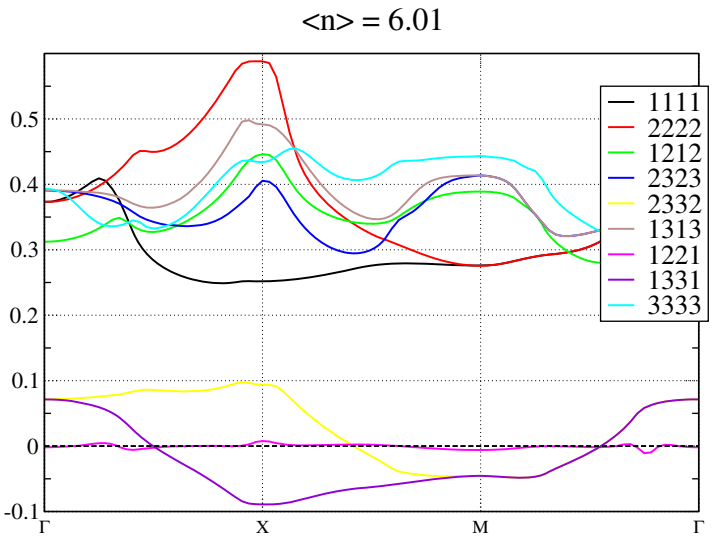

Figure A.3. The non-interacting susceptibilities $\chi^0_{\ell_1\ell_2\ell_3\ell_4}$ for $n = 6.01$.

In the same way, from the upper left 3×3 part of the interaction matrix, one obtains for example

$$\chi^{\mathrm{RPA}}_{1111} = \frac{\chi^0_1\left(\left(1-\bar{U}\chi^0_2\right)\left(1-\bar{U}\chi^0_3\right)-\bar{J}\chi^0_2\chi^0_3\right)}{D}, \tag{A.7}$$

where D is the determinant of $1 - U^s\chi^0$ and takes the form

$$D = \left(1-\bar{U}\chi^0_1\right)\left(1-\bar{U}\chi^0_2\right)\left(1-\bar{U}\chi^0_3\right) - \bar{J}^2\left(1-\bar{U}\chi^0_1\right)\chi^0_2\chi^0_3 - \bar{J}^2\left(1-\bar{U}\chi^0_2\right)\chi^0_1\chi^0_3$$
$$-\bar{J}^2\left(1-\bar{U}\chi^0_3\right)\chi^0_1\chi^0_2 - 2\bar{J}^3\chi^0_1\chi^0_2\chi^0_3, \tag{A.8}$$

with $\chi^0_a \equiv \chi^0_{aaaa}$. It is clear from these expressions that, for repulsive interactions and within the current approximation, while the intra-orbital spin susceptibilities depend on $\bar{U}$ and $\bar{J}$, the inter-orbital susceptibilities depend on $\bar{U}' \pm \bar{J}'$.

Although we have only kept the diagonal terms in the bare susceptibility, due to the structure of the interaction matrices there are off-diagonal terms in the RPA enhanced

susceptibility. From these components, we focus on the intra- and inter-orbital pair scattering processes, as the mixed-orbital processes are suppressed by the external matrix elements.

Within this diagonal bare susceptibility approximation, the inter-orbital pair scattering elements of Γ are simple because they involve only a 2×2 interaction matrix. For example, the pairing strength for the spin-fluctuation scattering of a d_{xz} pair to a d_{xy} pair is

$$\Gamma_{1331} = \frac{3}{4}\left[\frac{(\bar{U}'+\bar{J}')^2\chi^0_{13}}{1-(\bar{U}'+\bar{J}')\chi^0_{13}} - \frac{(\bar{U}'-\bar{J}')^2\chi^0_{13}}{1-(\bar{U}'-\bar{J}')\chi^0_{13}}\right]. \tag{A.9}$$

There is a corresponding Γ_{2332} element that describes the inter-orbital scattering of d_{yz} pairs from the α Fermi surfaces to the d_{xy} regions of the β_2 electron Fermi surface.

Since χ^0_{13} is associated with the nesting of the d_{xz} and d_{xy} parts of α_1 and β_1, respectively, it peaks for wave vectors near $(\pi, 0)$. For reasonable values of the pair hopping J', there can be a significant inter-orbital repulsive pair scattering from the d_{xz} regions of the hole Fermi surfaces α to the d_{xy} regions of the β Fermi surfaces. As $\bar{J}'$ goes to zero, the diagonal approximation for this inter-orbital d_{xz} to d_{xy} pair scattering vanishes linearly with $\bar{J}'$. If J' becomes small so that the neglected off-diagonal components of the susceptibility matrix χ^0_{1331} are large compared with $\frac{J'}{U'}\chi^0_{1313}$, then there will be off-diagonal corrections to Γ_{1313}. The leading correction is given by

$$\Gamma_{1331} \simeq \bar{U}'(\bar{U}'+2\bar{J})\chi^0_{1331}, \tag{A.10}$$

which gives the attractive interaction at $(\pi, 0)$ for $\bar{J} = \bar{J}' = 0$, as shown in figure 8.

In lowest order the $(\bar{U}')^2\chi^0_{1331}$ contribution comes from the second-order processes as seen in figure A.1. As seen in figure A.3, χ^0_{1331} is negative near the X point where $\mathbf{q} \simeq (\pi, 0)$.

The intra-orbital pair scattering involves a 3×3 matrix and is, in general, more complicated. However, in the diagonal susceptibility approximation, the intra-orbital Γ matrix will have the same determinant in the denominator as given by equation (A.8). From this, one can see how $\bar{U}$ and $\bar{J}$ enter in determining the intra-orbital pair scattering. In particular, the exchange $\bar{J}$ couples to the various bare susceptibilities such that, for example, the peak in χ^0_{2222} near X is reflected in Γ_{1111} and Γ_{3333} as well as Γ_{2222} when $\bar{J}$ is finite. To summarize, in the diagonal bare susceptibility approximation, the leading behavior of the intra-orbital pair scattering is controlled by $\bar{U}$ and $\bar{J}$. Increasing these interactions increases the repulsive scattering at $\mathbf{q} \sim (\pi, 0)$ and $(0, \pi)$. The leading behavior of the inter-orbital scattering is controlled by $\bar{U}'$ and $\bar{J}'$ and, in the diagonal bare susceptibility approximation, vanishes as $\bar{J}'$ goes to zero. When $\bar{J}'$ is small, the dominant contribution to the inter-orbital d_{xz} to d_{xy} and d_{yz} to d_{xy} scattering varies as $\bar{U}'(\bar{U}'+2J)\chi^0_{1331}$.

Appendix B. The orbital gauge

In the following section, we want to explicitly show that the choice of a gauge for the orbital basis does not affect the physical quantities, although one has to carefully take the orbital gauge into account when comparing orbital-dependent interaction parameters, such as e.g. the pair hopping term J'. First we define a gauge transformation of the orbital creation and annihilation operators as

$$\tilde{c}_{i\ell\sigma} = c_{i\ell\sigma}\, e^{i\phi_\ell}, \qquad \tilde{c}^\dagger_{i\ell\sigma} = c^\dagger_{i\ell\sigma}\, e^{-i\phi_\ell},$$

where $c^{\dagger}_{i\ell\sigma}$ creates a particle with spin σ in orbital ℓ at site i. Diagonalizing the non-interacting part of the Fourier-transformed Hamiltonian, the orbital phases can be absorbed into the matrix elements in the form

$$\tilde{c}_{\ell\sigma}(k) = \sum_{\nu} \tilde{a}^{\ell}_{\nu}(k)\psi_{\nu\sigma}(k),$$

where $\psi^{\dagger}_{\nu\sigma}(k)$ creates now a particle with spin σ and momentum k in band ν and the matrix element $\tilde{a}^{\ell}_{\nu}(k) = \mathrm{e}^{\mathrm{i}\phi_{\ell}} a^{\ell}_{\nu}(k)$. For the bare multiorbital susceptibility as defined in equation (A.5), we thus find the following transformation:

$$\tilde{\chi}^{0}_{\ell_1\ell_2\ell_3\ell_4}(q,\omega) = \chi^{0}_{\ell_1\ell_2\ell_3\ell_4}(q,\omega)\mathrm{e}^{\mathrm{i}(\phi_{\ell_1}-\phi_{\ell_2}-\phi_{\ell_3}+\phi_{\ell_4})},$$

while the spin susceptibility as an observable is gauge invariant

$$\tilde{\chi}_S(q) = \frac{1}{2}\sum_{\ell_1\ell_2} \tilde{\chi}^{0}_{\ell_1\ell_1\ell_2\ell_2}(q) = \chi_S(q).$$

If we now proceed to the interaction Hamiltonian equation (2), we note that the pair hopping term is not gauge invariant

$$\bar{J}' \sum_{i,\ell'\neq\ell} \tilde{c}^{\dagger}_{i\ell\uparrow}\tilde{c}^{\dagger}_{i\ell\downarrow}\tilde{c}_{i\ell'\downarrow}\tilde{c}_{i\ell'\uparrow} = \bar{J}' \sum_{i,\ell'\neq\ell} \mathrm{e}^{2\mathrm{i}(-\phi_{\ell}+\phi_{\ell'})} c^{\dagger}_{i\ell\uparrow}c^{\dagger}_{i\ell\downarrow}c_{i\ell'\downarrow}c_{i\ell'\uparrow}$$

and we can define the gauge transformation for $\bar{J}'$ as

$$\tilde{\bar{J}}' = \mathrm{e}^{2\mathrm{i}(-\phi_{\ell}+\phi_{\ell'})}\bar{J}'.$$

Using this relation allows us to write the gauge transformed interaction matrices as

$$\tilde{U}^{s/c}_{\ell_1\ell_2\ell_3\ell_4} = U^{s/c}_{\ell_1\ell_2\ell_3\ell_4}\mathrm{e}^{\mathrm{i}(\phi_{\ell_1}-\phi_{\ell_2}-\phi_{\ell_3}+\phi_{\ell_4})}.$$

It is straightforward to show that this relation also yields the correct gauge transformation for the RPA enhanced multiorbital susceptibility

$$\tilde{\chi}^{\mathrm{RPA}}_{1}(q) = \tilde{\chi}^{0}(q) + \tilde{\chi}^{\mathrm{RPA}}_{1}(q)\tilde{U}^{s}\tilde{\chi}^{0}(q)$$

with

$$(\tilde{\chi}^{\mathrm{RPA}}_{1})_{\ell_1\ell_2\ell_3\ell_4}(q,\omega) = (\chi^{\mathrm{RPA}}_{1})_{\ell_1\ell_2\ell_3\ell_4}(q,\omega)\,\mathrm{e}^{\mathrm{i}(\phi_{\ell_1}-\phi_{\ell_2}-\phi_{\ell_3}+\phi_{\ell_4})};$$

under this transformation, the orbital-dependent pairing vertex (equation (3)) transforms as

$$\tilde{\Gamma}_{\ell_1\ell_2\ell_3\ell_4}(k,k',\omega) = \Gamma_{\ell_1\ell_2\ell_3\ell_4}(k,k',\omega)\mathrm{e}^{-\mathrm{i}(\phi_{\ell_1}-\phi_{\ell_2}-\phi_{\ell_3}+\phi_{\ell_4})}$$

and we see that the effective pairing vertex entering the linearized gap equation is gauge invariant.

In the above, we have presented the orbital pairing vertices (in figures 5, 8 and 9) and orbital susceptibilities (in figure A.3). Both these quantities depend on the choice of orbital gauge. We have chosen to present them in the basis where (1) the d_{xz} and d_{yz} orbitals are aligned along the Fe–Fe directions and (2) none of the orbitals have a purely imaginary phase with respect to any other. In the notation above, $\phi_{\ell} = 0$, for all ℓ. In this basis, $a^{l}_{\nu}(-\mathbf{k}) = a^{l*}_{\nu}(\mathbf{k})$, so that the sign of the intra- and inter-orbital pairing vertices accurately reflects their contribution to the gauge invariant pairing vertex $\Gamma_{ij}(\mathbf{k},\mathbf{k}')$.

References

[1] Kamihara Y, Watanabe T, Hirano M and Hosono H 2008 *J. Am. Chem. Soc.* **130** 2396
[2] Ishida K, Nakai Y and Hosono H 2009 *J. Phys. Soc. Japan* **78** 062001
[3] Kuroki K, Onari S, Arita R, Usui H, Tanaka Y, Kontani H and Aoki H 2008 *Phys. Rev. Lett.* **101** 087004
[4] Graser S, Maier T A, Hirschfeld P J and Scalapino D J 2009 *New J. Phys.* **11** 025016
[5] Lebègue S 2007 *Phys. Rev.* B **75** 035110
[6] Singh D J and Du M-H 2008 *Phys. Rev. Lett.* **100** 237003
[7] Cao C, Hirschfeld P J and Cheng H-P 2006 *Phys. Rev.* B **77** 220506
[8] Zhao L *et al* 2008 *Chin. Phys. Lett.* **25** 4402
[9] Ding H *et al* 2008 *Europhys. Lett.* **83** 47001
[10] Kondo T *et al* 2008 *Phys. Rev. Lett.* **101** 147003
[11] Evtushinsky D *et al* 2009 *Phys. Rev.* B **79** 054517
[12] Nakayama K *et al* 2009 *Europhys. Lett.* **85** 67002
[13] Wray L *et al* 2008 *Phys. Rev.* B **78** 184508
[14] Mazin I I, Singh D J, M D and Johannes Du M H 2008 *Phys. Rev. Lett.* **101** 057003
[15] Dong J *et al* 2008 *Europhys. Lett.* **83** 27006
[16] Christianson A D *et al* 2008 *Nature* **456** 930
[17] Lumsden M D *et al* 2009 *Phys. Rev. Lett.* **102** 107005
[18] Chi S X *et al* 2000 *Phys. Rev. Lett.* **102** 107006
[19] Maier T A and Scalapino D J 2008 *Phys. Rev.* B **78** 020514
[20] Korshunov M M and Eremin I 2008 *Europhys. Lett.* **83** 67003
[21] Maier T A, Graser S, Scalapino D J and Hirschfeld P 2009 *Phys. Rev.* B **79** 134520
[22] Fletcher J D, Serafin A, Malone L, Analytis J G, Chu J-H, Erickson A S, Fisher I R and Carrington A 2009 *Phys. Rev. Lett.* **102** 147001
[23] Hicks C W, Lippman T M, Huber M E, Analytis J G, Chu J-H, Erickson A S, Fisher I R and Moler K A 2009 *Phys. Rev. Lett.* **103** 127003
[24] Hashimoto K *et al* 2010 *Phys. Rev.* B **81** 220501
[25] Gordon R T, Martin C, Kim H, Ni N, Tanatar M A, Schmalian J, Mazin I I, Bud'ko S L, Canfield P C and Prozorov R 2009 *Phys. Rev.* B **79** 100506
[26] Klingeler R, Leps N, Hellmann I, Popa A, Hess C, Kondrat A, Hamann-Borrero J, Behr G, Kataev V and Buechner B 2010 *Phys. Rev.* B **81** 024506
[27] Matano K, Ren Z A, Dong X L, Sun L L, Zhao Z X and qing Zheng G 2008 *Europhys. Lett.* **83** 57001
[28] Grafe H- J 2008 *Phys. Rev. Lett.* **101** 047003
[29] Ahilan K, Ning F, Imai T, Sefat A, Jin R, McGuire M, Sales B and Mandrus D 2008 *Phys. Rev.* B **78** 100501
[30] Nakai T Y *et al* 2008 *J. Phys. Soc. Japan* **77** 073701
[31] Yashima M, Nishimura H, Mukuda H, Kitaoka Y, Miyazawa K, Shirage P M, Kiho K, Kito H, Eisaki H and Iyo A 2009 *J. Phys. Soc. Japan* **78** 103702
[32] Luo X G *et al* 2009 *Phys. Rev.* B **80** 140503
[33] Yamashita M, Nakata N, Senshu Y, Tonegawa S, Ikada K, Hashimoto K, Sugawara H, Shibauchi T and Matsuda Y 2009 *Phys. Rev.* B **80** 220509
[34] Checkelsky J G, Li L, Chen G F, Luo J L, Wang N L and Ong N P 2008 arXiv:0811.4668
[35] Tanatar M A, Reid J P, Shakeripour H, Luo X G, Doiron-Leyraud N, Ni N, Bud'ko S L, Canfield P C, Prozorov R and Taillefer L 2010 *Phys. Rev. Lett.* **104** 067002
[36] Machida Y, Tomokuni K, Isono T, Izawa K, Nakajima Y and Tamegai T 2008 arXiv:0906.0508
[37] Ding L *et al* 2009 *New J. Phys.* **11** 093018
[38] Muschler B, Prestel W, Hackl R, Devereaux T P, Analytis J G, Chu J-H and Fisher I R 2009 *Phys. Rev.* B **80** 180510
[39] Golubov A A and Mazin I I 1997 *Phys. Rev.* B **55** 15146

[40] Wang F, Zhai H, Ran Y, Vishwanath A and Lee D-H 2009 *Phys. Rev. Lett.* **102** 047005
[41] Maier T A, Graser S, Scalapino D J and Hirschfeld P J 2009 *Phys. Rev.* B **79** 224510
[42] Kuroki K, Usui H, Onari S, Arita R and Aoki H 2009 *Phys. Rev.* B **79** 224511
[43] Vildosola V, Pourovskii L, Arita R, Biermann S and Georges A 2008 *Phys. Rev.* B **78** 064518
[44] Calderon M J, Valenzuela B and Bascones E 2009 *Phys. Rev.* B **80** 094531
[45] Chubukov A V, Vavilov M G and Vorontsov A B 2009 *Phys. Rev.* B **80** 140515
[46] Thomale R, Platt C, Hu J, Honerkamp C and Bernevig B A 2009 *Phys. Rev.* B **80** 180505
[47] Ikeda H, Arita R and Kuneš J *Phys. Rev.* B **81** 054502
[48] Ikeda H, Arita R and Kuneš J 2010 arXiv:1002.4471
[49] Wang F, Zhai H and Lee D-H 2010 *Phys. Rev.* B **81** 184512
[50] Thomale R, Platt C, Hanke W and Bernevig B A 2008 arXiv:1002.3599
[51] Zhang J, Sknepnek R, Fernandes R M and Schmalian J 2009 *Phys. Rev.* B **79** 220502
[52] Bickers N E, Scalapino D J and White S R 1989 *Phys. Rev. Lett.* **62** 961
[53] Kubo K 2007 *Phys. Rev.* B **75** 224509
[54] Giannozzi P *et al* 2009 *J. Phys.: Condens. Matter* **21** 395502
[55] Perdew J P, Burke K and Ernzerhof M 1996 *Phys. Rev. Lett.* **77** 3865
[56] Sakakibara H, Usui H, Kuroki K, Arita R and Aoki H 2010 arXiv:1003.1770